AGU PUBLICATIONS

JGR

Journal of Geophysical Research: Space Physics

RESEARCH ARTICLE
10.1002/2016JA023354

Key Points:
- Numerical modeling shows that lightning stroke excites coupled system of IAR and FMS waveguide
- In lightning proximity (about few hundred kilometers) only lowest IAR harmonics are stimulated
- At distances larger than 800 km multiband spectral structure is formed by harmonics of FMS waveguide

Correspondence to:
V. Pilipenko,
space.soliton@gmail.com

Citation:
Fedorov, E., N. Mazur, V. Pilipenko, and L. Baddeley (2016), Modeling the high-latitude ground response to the excitation of the ionospheric MHD modes by atmospheric electric discharge, *J. Geophys. Res. Space Physics*, *121*, doi:10.1002/2016JA023354.

Received 17 AUG 2016
Accepted 16 OCT 2016
Accepted article online 24 OCT 2016

Modeling the high-latitude ground response to the excitation of the ionospheric MHD modes by atmospheric electric discharge

E. Fedorov[1], N. Mazur[1], V. Pilipenko[1,2], and L. Baddeley[3]

[1]Institute of Physics of the Earth, Moscow, Russia, [2]Space Research Institute, Moscow, Russia, [3]Birkeland Centre for Space Science, University Centre in Svalbard, Longyearbyen, Norway

Abstract The ionospheric Alfvén resonator (IAR) and fast magnetosonic (FMS) waveguide, which can trap the electromagnetic wave energy in the range from fractions of Hz to several Hz, are characteristic features of the upper ionosphere. Their role in the electromagnetic impulsive coupling between atmospheric discharge processes and the ionosphere can be elucidated with a proper model. The presented model is based on numerical solution of coupled wave equations for electromagnetic modes in the ionosphere and atmosphere in a realistic ionosphere modeled with the use of IRI (International Reference Ionosphere) vertical profiles. The geomagnetic field is supposed to be nearly vertical, so the model can be formally applied to high latitudes, though the main features of ground ULF structure will be qualitatively similar at middle latitudes as well. The modeling shows that during the lightning discharge a coupled wave system comprising IAR and MHD waveguide is excited. Using the model, the spatial structure, frequency spectra, and polarization parameters have been calculated at various distances from a vertical dipole. In the lightning proximity (about several hundred kilometer) only the lowest IAR harmonics are revealed in the radial magnetic component spectra. At distances >800 km the multiband spectral structure is formed predominantly by harmonics of FMS waveguide modes. The model predictions do not contradict the results of search coil magnetometer observations on Svalbard; however, the model validation demands more dedicated experimental studies.

1. Introduction

Atmospheric thunderstorms and lightning constitute one of the most powerful electromagnetic disturbances in the Earth's environment and provide the possibility of impulsive coupling of the atmosphere with the ionosphere/magnetosphere. Lightning is the natural source of broadband electromagnetic emission in ULF-ELF-VLF-HF frequency bands from ~0.1 Hz to ~30 MHz. The largest spectral density of such emissions is concentrated in the VLF band (a few kHz), though a contribution of high frequencies into an observed spectrum decreases with distance. However, an essential power is contained in the lower ELF-ULF bands (from fractions of Hz to tens of Hz). For example, magnetic impulses in the frequency range of about several Hz were revealed at distances up to several thousand kilometers from a stroke [*Bösinger et al.*, 2006].

A characteristic feature of the geomagnetic variations in the ULF band, just below the fundamental tone of the Schumann resonance (~8 Hz), is a multiband spectral resonant structure during nighttime hours (see more complete set of references in reviews by *Demekhov* [2012], *Pilipenko* [2012], and *Surkov and Hayakawa* [2014]). The occurrence of this spectral structure was commonly attributed to the Ionospheric Alfvén Resonator (IAR) in the upper ionosphere. This resonator is formed owing to an Alfvén wave partial reflection from the bottomside ionosphere and a steep gradient of the Alfvén velocity vertical profile $V_A(z)$ above the maximum of the *F* layer at altitude of $\sim 10^3$ km. The ionospheric cavity with minimum of $V_A(z)$ in the *F* layer functions not only as a resonator for Alfvén waves but also as a waveguide for the fast magnetosonic (FMS) mode. Trapped FMS waveguide modes can propagate to large distances (up to a few thousand kilometers) along the ionosphere [*Greifinger and Greifinger*, 1968; *Pilipenko et al.*, 2011]. In the frequency domain, the ionospheric wave guidance manifests itself as an occurrence of cutoff frequency corresponding to the FMS waveguide critical frequency.

An adequate interpretation of multiband spectral structure regularly observed on the ground during night time ("hydromagnetic spectroscopy of the upper ionosphere") on the basis of a quantitative model enables a ground observer to monitor the *F* layer peak density [*Potapov et al.*, 2014; *Baru et al.*, 2014]. The needed spectral properties of the IAR (eigenfrequencies and damping rates) were well reproduced by numerous analytical and numerical models which will be reviewed below. The quality factors *Q* of the IAR modes strongly depend on the Alfvén velocity differential in the upper ionosphere and on the lower ionosphere conductivity. A smooth vertical profile $V_A(z)$ is one of the main reasons of the suppression of IAR excitation during daytime hours and periods of high solar activity [*Trakhtengertz et al.*, 2000]. At the same time, a physical mechanism of the IAR excitation has not been firmly established yet. At auroral latitudes, magnetospheric wideband electromagnetic disturbances can produce multiple spectral bands on the ground due to resonant transmissive properties of the ionosphere in the IAR band [*Fedorov et al.*, 2014]. The most promising energy source for the IAR excitation at middle and low latitudes might be related to atmospheric lightning discharges: either world thunderstorm centers in the tropics [*Belyaev et al.*, 1989; *Bösinger et al.*, 2002], regional thunderstorms [*Fedorov et al.*, 2006; *Surkov et al.*, 2006], or even high-altitude electric discharges [*Sukhorukov and Stubbe*, 1997]. Thus, the kind of thunderstorms that drive the multiband spectral structure is still disputable.

Extensive searches for IAR multiband signatures at very high latitudes [*Semenova et al.*, 2008] provided a number of interesting but still not well-comprehended results. While the probability to observe the multiband spectral structure during night hours reaches nearly 100% at low latitudes, and ∼80% at middle latitudes [*Ermakova et al.*, 2008], on Svalbard (the polar cap Barentsburg observatory) the probability is ∼40% [*Semenova and Yahnin*, 2008]. Time variations of spectral band frequencies were much weaker than variations at middle/low latitudes. At middle/low latitudes the multiband spectral structure is a typical nighttime phenomenon. Its absence during daytime hours was interpreted as evidence of the IAR low quality and enhanced *E* layer absorption in the dayside ionosphere. However, on Svalbard the multiband spectral structure was not observed in nominal daytime hours even during polar night months. Moreover, this spectral structure was observed during winter months less frequently than during summer. These observational facts made *Semenova et al.* [2008] to conclude that solar illumination is not a decisive factor of the IAR signature occurrence at polar latitudes, in contrast to middle/low latitudes.

Here we present a numerical model to estimate the spectral-spatial structure of magnetic perturbations driven by a separate lightning discharge at a very high latitude, where the geomagnetic field is vertical (inclination angle $I \to 90°$). The specific features of the proposed model and its distinction from earlier models are discussed in the next chapter.

2. Earlier Models of the IAR Excitation by Lightning

The modeling of the electromagnetic excitation of the atmosphere-ionosphere system by an atmospheric electric dipole was started by a seminal paper by *Polyakov and Rapoport* [1981]. The influence of IAR on the ground electromagnetic field was examined originally in the frameworks of models, where the bottom ionosphere was modeled as a thin current sheet with height-integrated Pedersen and Hall conductances [e.g., *Polyakov et al.*, 2003]. Then, more realistic profiles of the ULF wave refraction index were derived from various ionospheric models [e.g., *Ermakova et al.*, 2008; *Bösinger et al.*, 2009; *Mursula et al.*, 2000; *Lysak et al.*, 2013].

A series of models were derived [e.g., *Polyakov and Rapoport*, 1981; *Belyaev et al.*, 1989] utilizing analytical relationships from *Sobchakov et al.* [2003] for the ground magnetic response to an emitting dipole in a quasi-static limit in the waveguide between the Earth surface and the bottom ionosphere with a frequency-dependent impedance. Later, incorporating the surface impedance of the upper waveguide boundary (ionosphere), the ground magnetic ULF response was estimated for an inclined geomagnetic field [*Ermakova et al.*, 2008]. The input impedance of the lower ionosphere (upper boundary of the atmospheric waveguide) was determined by the IAR spectral properties, calculated using the vertical structure of the ionosphere derived either from the IRI model or from the Chapman layer approximation. The source of electromagnetic noise in the ULF band was assumed to be a vertical electric dipole at distance ρ from an observation site. The primary electromagnetic field was produced by atmospheric zero mode in a quasi-static approximation; therefore, all the spectral features did not depend on distance, but the amplitude of the IAR response monotonically decreased with distance from a stroke as ρ^{-1}. Changes in the topside ionospheric profile, geomagnetic field inclination, and direction toward a source resulted in different modulation depths of ground spectra and asymmetry between spectral peaks in the *H* and *D* components.

Special attention was paid to the signal polarization, namely, ellipticity $\kappa(f)$. This parameter is often used to highlight the IAR structure, because it does not depend on a source spectrum and frequency response of the recording system. The ellipticity κ was shown to depend on the admittance of the ionosphere, but it did not depend on the direction to a source and was determined only by local properties of the ionosphere [*Polyakov et al.*, 2003; *Ermakova et al.*, 2010].

Semenova et al. [2008] attempted to interpret observations of the multiband spectral emissions at polar latitudes (Svalbard) by numerically calculating the Alfvén wave reflection coefficient $R(f)$ for a realistic ionosphere. The ionospheric parameters were derived from the statistical ISRIM model based on European Incoherent Scatter (EISCAT) radar observations on Svalbard. Thus, the authors implicitly assumed that the resonant structure is driven by a magnetospheric source. In contrast to observations, these calculations showed no significant seasonal or daily dependence of $R(f)$ modulation. Therefore, the mechanism of multiband spectral features at polar latitudes still remains unresolved.

However, in all earlier studies an excitation of waveguide FMS modes was neglected, though a linear coupling of shear Alfvén and FMS modes in an anisotropically conducting plasma was known [e.g., *Surkov et al.*, 2004]. Contrary to that, we suppose that during the impact of the atmospheric electric discharge fields on the ionosphere not just a local IAR is to be excited but a more global wave structure, comprising both IAR and FMS waveguide, is stimulated.

3. A New Model of the ULF Emission Generation by an Atmospheric Electric Discharge

A typical cloud-to-ground (CG^-) negative lightning discharge starts with a downward stepwise-propagating leader, then a subsequent upward propagating return stroke produces a main breakdown of the atmosphere between the ground and cloud, carrying the negative charge Q of about a few tens of Coulombs to the ground. More rare, but more intense, positive CG^+ discharges carry about an order of magnitude larger positive charge to the ground. A vertical CG stroke is a more effective source of electromagnetic fields in the Earth-ionosphere cavity than horizontal intracloud strokes. A lightning stroke can be mimicked as a current moment $M_C(t) = I(t)L(t) + L(t)\partial_t Q(t) \simeq I(t)L(t)$, where $I(t)$ is the current and $L(t)$ is the lightning channel length [*Nickolaenko and Hayakawa*, 2002]. A current moment is the time derivative of a charge moment, $M_C = -\partial_t M_Q$, where $M_Q = QL$. Most lightning flashes are composed of several strokes that have a channel to the ground in which a current flows on the order of 1 ms. However, there exists a class of flashes in which one or more strokes sustain a continuing current, i.e., a stroke in which a luminous conductive channel exists for tens of milliseconds and more. About 25% CG^- lightning flashes contain a long (mean duration 115 ms) continuing current and ~15% contain a short (mean duration 23 ms) continuing current with average amplitudes in the range 30–200 A [*Shindo and Uman*, 1989]. The lightning flashes with a continuing current are most effective generators of electromagnetic power in the ULF band. Positive CG^+ discharges can be of primary importance in excitation of the IAR since their charge moment and continuing current are, on average, larger than those of CG^- discharges [*Shalimov and Bösinger*, 2008].

An adequate description of the atmosphere-ionosphere coupling demands a comprehensive consideration of all electromagnetic modes involved. The electromagnetic field in the atmosphere is composed of partial electric (E) and magnetic (H) modes, whereas in the ionosphere the wavefield is composed of Alfvén and FMS modes. The primary field excited by a vertical electric dipole (stroke) in the atmosphere is carried by the E mode. In a cylindrical coordinate system $\{\rho, \varphi, z\}$ with vertical z axis this mode has electric components E_ρ, E_z, and an azimuthal magnetic component b_φ. Another H mode has an electric component E_φ, and radial and vertical magnetic components, b_ρ and b_z. In the ionosphere the Alfvén mode is partially trapped into the IAR and partially leaks into the magnetosphere. The FMS mode is partially dispersed throughout the outer space, but a part of its energy can be trapped in the ionospheric waveguide and thus be transmitted along the ionosphere. In an anisotropically conductive ionosphere with inclined geomagnetic field, all modes are coupled.

On a qualitative basis the response of the ionosphere to an atmospheric electric discharge may be outlined as follows [e.g., *Belyaev et al.*, 1989; *Fedorov et al.*, 2014]. A stroke generates an initial E mode pulse which propagates in the ionosphere-ground waveguide. The magnetic component b_φ of this pulse is orthogonal to the direction toward a source. Upon interaction of the initial E pulse with the anisotropic lower ionosphere, the atmospheric H mode is excited also. Therefore, a pulse reflected from the ionosphere holds an additional magnetic component b_ρ, directed toward a source. Both direct and reflected pulses in ULF-ELF frequency range almost simultaneously reach an observation site and are recorded as a primary pulse. Meanwhile, the E pulse partially penetrates into the ionosphere, travels up the ionosphere as an Alfvén pulse, and reflects back from the upper IAR boundary. This pulse returns to the ground as an echo pulse in the H mode owing to the mode conversion in the lower ionosphere. The delay between the echo pulse and the primary pulse is about the time of the Alfvén wave propagation up and down in the ionospheric cavity, that is about the fundamental IAR eigenperiod. Ionospheric FMS waveguide mode cannot be directly excited by a vertical stroke in the atmosphere, but the mode coupling in the lower ionosphere results in its excitation. The waveguide modes convey a part of the wave energy away from an excitation region along the ionosphere. Even this qualitative scheme indicates that an observed time-space structure of the electromagnetic response to an atmospheric discharge is a complicated interference pattern of various modes, and its adequate description is impossible without numerical modeling. The basics of such a model are outlined here.

The axis z of the Cartesian coordinate system is chosen to be vertical upward with $z = 0$ on the ground, whereas x is southward, and y is eastward. We also use the cylindrical coordinate system $\{\rho, \varphi, z\}$, where the azimuthal angle φ is measured from the x axis in a positive direction (the direction from a source northward corresponds to $\varphi = 180°$). The dipole source is situated at the altitude $z = z_d$. Formally, a source can be at any altitude z_d in the atmosphere.

The ionosphere is assumed to be horizontally stratified; that is, the tensors of conductivity $\hat{\sigma}(z,\omega)$ and relative dielectric permittivity $\hat{\varepsilon}(z,\omega) = i\hat{\sigma}(z,\omega)/\omega\varepsilon_0$ depend on altitude z only. The atmospheric slab with realistic conductivity and permittivity profiles, $\sigma_a(z)$ and $\varepsilon_a(z) = 1 + i\sigma_a(z)/\omega\varepsilon_0$, taken from *Nickolaenko et al.* [2015], is bounded by the conductive ground at $z = 0$ and by the bottom ionosphere at $z = d$. The ground is assumed to be a uniform conductor with conductivity σ_g. The vertical profiles of the ionospheric parameters are reconstructed utilizing the IRI and MSIS models [*Bilitza and Reinisch*, 2008]. From the local plasma parameters given by the IRI model the vertical distribution of $\hat{\varepsilon}(z)$ and $\hat{\sigma}(z)$ are deduced. We do not impose a usual condition that field-aligned conductivity in the ionosphere is infinite. Thanks to that, a transition from strongly anisotropic ionosphere to the isotropic atmosphere is smooth. The ionospheric plasma is assumed to be immersed in the homogeneous vertical geomagnetic field $\mathbf{B}_0$ (inclination angle $I = 90°$). This assumption is reasonable for high-latitude observations.

4. Spatial Fourier Components of the Electromagnetic Field Generated by a Localized Current Source

The Maxwell's equations for the wave harmonic of magnetic field $\mathbf{b} \propto \exp(-i\omega t)$ and electric (normalized to the light velocity c) field $\mathbf{e} = \mathbf{E}/c \propto \exp(-i\omega t)$ are as follows:

$$\nabla \times \mathbf{e} = ik_0\mathbf{b}, \quad \nabla \times \mathbf{b} = -ik_0\hat{\varepsilon}\mathbf{e} + \mu_0\mathbf{j}_d \,. \tag{1}$$

Here $k_0 = \omega/c$ is the free-space wave number, $\varepsilon_0\hat{\varepsilon}$ is the tensor of complex-valued permittivity, $\hat{\varepsilon}$ is the relative complex-valued permittivity tensor, ε_0 is the vacuum permittivity, and $\mathbf{j}_d$ is the external current density produced by a stroke. In a Cartesian coordinate system oriented along the geomagnetic field $\mathbf{B}_0$, the tensor of relative dielectric permittivity (normalized to ε_0) has a form

$$\hat{\varepsilon} = \begin{pmatrix} \varepsilon_\perp & ig & 0 \\ -ig & \varepsilon_\perp & 0 \\ 0 & 0 & \varepsilon_\parallel \end{pmatrix}. \tag{2}$$

Cumbersome expressions for the tensor (2) diagonal $\varepsilon_\perp$, off-diagonal g, and parallel $\varepsilon_\parallel$ components can be found in *Ginzburg* [1970]. We consider frequencies in ULF frequency band, lower than the frequency of the Schumann resonance fundamental tone. We also neglect the Earth surface curvature, so electromagnetic disturbances do not produce a noticeable world-around ULF echo. The distances to a source are assumed to be large as compared with the typical scale of lightning channel L, $\rho \gg L$ (~1–10 km). Therefore, the external current may be modeled as a point dipole. Magnetic disturbance produced by a horizontal dipole decays with distance as $\propto \rho^{-2}$, whereas from a vertical dipole it decays as $\propto \rho^{-1}$. Therefore, at large distances from a source a contribution from the horizontal component of the discharge current may be neglected. Thus, the external current density and its Fourier transform can be modeled as a point vertical dipole

$$\mathbf{j}_d(\mathbf{r},t) = \mathbf{M}_C(t)\delta(\mathbf{r} - z_d\hat{\mathbf{z}}), \qquad \mathbf{j}_d(\mathbf{r},\omega) = -\Delta\mathbf{M}_Q\delta(\mathbf{r} - z_d\hat{\mathbf{z}})\hat{\mathbf{z}}, \tag{3}$$

where $\hat{\mathbf{z}}$ is the vertical unit vector, and r is the position vector.

A duration of lightning stroke is much less that the time scale of ULF disturbances under consideration. Therefore, we may suppose that the current moment $\mathbf{M}_C(t) = -\Delta\mathbf{M}_Q\delta(t)\hat{\mathbf{z}}$, where $\Delta\mathbf{M}_Q$ is the variation of the charge moment during a stroke. The Fourier transform of the current moment $\mathbf{M}_C(t)$ does not depend on frequency, and it is equal to the variation of the charge moment, $\mathbf{M}_C(\omega) = -\Delta\mathbf{M}_Q$.

The refraction coefficients for Alfvén and FMS modes, $n^{(A)}$ and $n^{(F)}$, can be determined from the solution of local dispersion biquadratic equation for a cold magnetized collisional plasma, which has the form $n^4 + Pn^2 + Q = 0$. The coefficients of this equation depend on ω, $k_\perp$ and the components of the tensor (2) and have the explicit form as follows: $P = \left(1 + \varepsilon_\perp U^{-1}\right) q_\perp^2 - 2\varepsilon_\perp$, $Q = \varepsilon_\perp^2 - g^2 - \left[\varepsilon_\perp + \left(\varepsilon_\perp^2 - g^2\right) U^{-1}\right] q_\perp^2 + \varepsilon_\perp U^{-1} q_\perp^4$, where $U = \varepsilon_\perp \cos^2 I + \varepsilon_\parallel \sin^2 I$ and $q_\perp = k_\perp / k_0$.

The vertical structure of real Re(n) and imaginary Im(n) parts for vertically incident waves ($k_\perp = 0$) is shown in Figure 1 for 1 and 6 Hz frequencies. This figure shows the occurrence of several regions with steep gradients of $n^{(A)}(z)$: in the upper ionosphere above F layer ($z > 400$ km) and beneath F layer ($z \simeq 250-300$ km). The E layer is another reflecting boundary. These gradients result in formation of two possible Alfvénic quasi-resonators: the IAR between the E layer and upper ionosphere, and sub-IAR in the valley between the E and F layers [*Ermakova et al.*, 2007]. The imaginary part Im($n^{(A)}$) is significant in the valley; therefore, the Q factor of sub-IAR should not be high.

The wave equations for coupled Alfvén and FMS modes in a collisional plasma can be found in *Fedorov et al.* [2016]. Here we present the system of Maxwell's equation (1) in an oblique-angled coordinate system $\{x^1, x^2, x^3\}$ for the covariant components of magnetic $\{b_1, b_2, b_3\}$ and electric $\{e_1, e_2, e_3\}$ fields in a matrix form. We apply the Fourier transform to the dependence on horizontal coordinates $\boldsymbol{\rho} = (x^1, x^2)$ and exclude from Fourier transform equations the field-aligned components b_3 and e_3. The spatial harmonics of transverse magnetic, $\mathbf{b}_\tau(\rho, x^3, \omega) \to \mathbf{b}_\tau(\mathbf{k}_\tau, x^3, \omega)$, and electric, $\mathbf{e}_\tau(\rho, x^3, \omega) \to \mathbf{e}_\tau(\mathbf{k}_\tau, x^3, \omega)$, fields, excited by a source at altitude $z = z_d$, are described by the following system:

$$\partial_3 \mathbf{b}_\tau = \mathbf{T}^{\mathrm{bb}}\mathbf{b}_\tau + \mathbf{T}^{\mathrm{be}}\mathbf{e}_\tau + \mathbf{s}_b\delta\left(x^3 - z_d\right), \tag{4}$$

$$\partial_3 \mathbf{e}_\tau = \mathbf{T}^{\mathrm{eb}}\mathbf{b}_\tau + \mathbf{T}^{\mathrm{ee}}\mathbf{e}_\tau + \mathbf{s}_e\delta\left(x^3 - z_d\right), \tag{5}$$

where $\mathbf{b}_\tau = (b_1, b_2)$, $\mathbf{e}_\tau = (e_1, e_2)$ and $\mathbf{k}_\tau = (k_1, k_2)$. The formulas for the matrices $\mathbf{T}^{\mathrm{bb}}$, $\mathbf{T}^{\mathrm{be}}$, $\mathbf{T}^{\mathrm{eb}}$, and $\mathbf{T}^{\mathrm{ee}}$, as well as for the source vectors $\mathbf{s}_b$ and $\mathbf{s}_e$, are given in Appendix B.

The equations (4) and (5) are to be augmented by boundary conditions. Only decaying at $x_3 \to \infty$ solutions have a physical sense. At the ground ($z = 0$) the wave electric and magnetic components are related by the impedance condition [*Budden*, 1966]

$$\mathbf{e}_\tau(\mathbf{k}_\tau, 0, \omega) = \mathbf{Z}_g(\mathbf{k}_\tau, \omega)\mathbf{b}_\tau(\mathbf{k}_\tau, 0, \omega), \tag{6}$$

where $\mathbf{Z}_g(\mathbf{k}_\tau, \omega) = \boldsymbol{\zeta}(\mathbf{k}_\tau, \omega)/Z_0$ is the surface spectral impedance matrix normalized by the impedance of a free space $Z_0 = \sqrt{\mu_0/\varepsilon_0}$. Here $\boldsymbol{\zeta}$ is impedance matrix, stemming from the relationship $\mathbf{E}_\tau = \boldsymbol{\zeta}\mu_0^{-1}\mathbf{b}_\tau$. If the strong skin effect condition is fulfilled, $k_\tau\delta_g \ll 1$, where $\delta_g = \sqrt{i\omega\mu_0\sigma_g}$ is the characteristic skin depth, then $\mathbf{Z}_g(\mathbf{k}_\tau, \omega) \simeq \mathbf{Z}_g(0, \omega) = \mathbf{Z}_g^0$. For a homogeneous half-space with conductivity $\sigma_g = $ const normalized impedance $\mathbf{Z}_g^0$ is an antidiagonal matrix, $\mathbf{Z}_g^0 = (0, -\varepsilon_g^{-1/2}; \varepsilon_g^{-1/2}, 0)$, where $\varepsilon_g = \mathrm{Re}\,\varepsilon_g + \sigma_g/\omega\varepsilon_0$.

The external source (stroke) is located at altitude $z = z_d$ inside the atmosphere with isotropic conductivity; that is, the elements of the tensor (2) are $\varepsilon_\perp = \varepsilon_\parallel = \varepsilon$, and $g = 0$. As a result, the inhomogeneous terms in (4) vanish, $\mathbf{s}_b = 0$. The relationship between the fields beneath and above a source can be found by integrating the equations (4) and (5) along a field line (coordinate x^3) over a region occupied by a source, as follows:

$$\{\mathbf{b}_\tau\}_{z_d} = 0, \quad \{\mathbf{e}_\tau\}_{z_d} = S_0\mathbf{k}_\tau, \quad S_0 = \frac{\mu_0 M_C(\omega)}{2\pi k_0 \varepsilon(z_d)}. \tag{7}$$

Here $\{\dots\}$ denote a jump of a function $f(z)$ at $z = z_d$: $\{f\}_{z_d} = f(z_d + 0) - f(z_d - 0)$.

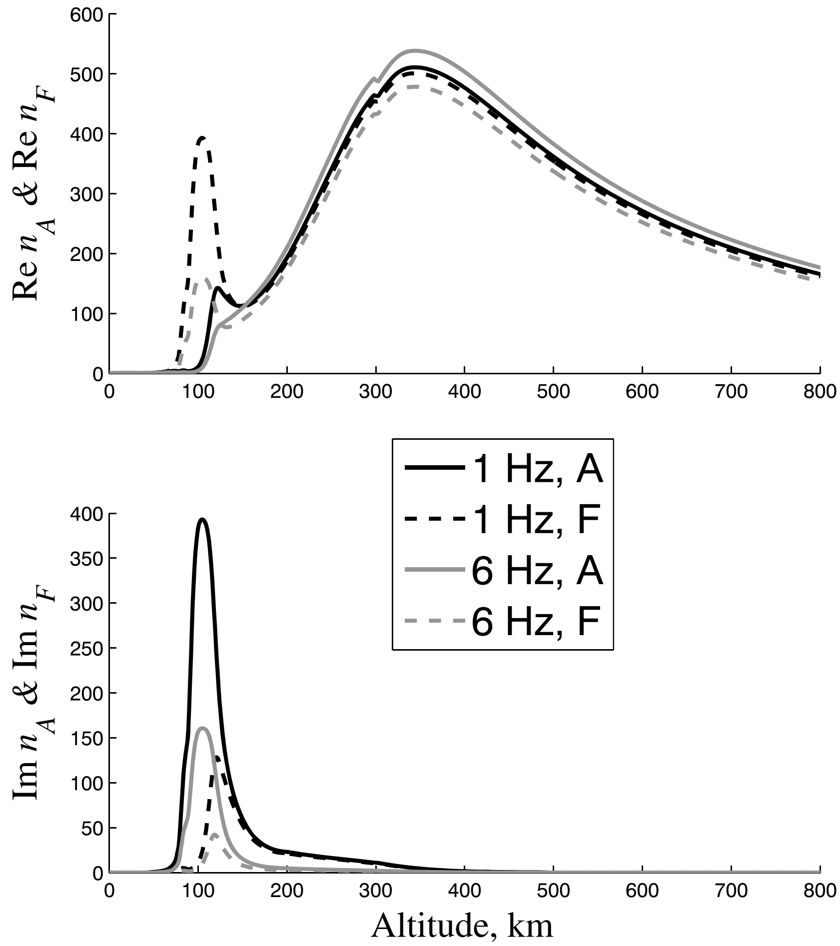

Figure 1. The vertical structure of local refraction coefficients for Alfvén and FMS modes, $n^{(A)}(z)$ and $n^{(F)}(z)$: (top) real part and (bottom) imaginary part for vertically incident waves ($k_\perp = 0$) for preselected frequencies 1 and 6 Hz.

Using these relationships, one can find a spatial spectrum (the Fourier transform) of the horizontal electromagnetic field components at the source level $z = z_d$. Mathematical details are given in Appendix A, and the result is

$$\mathbf{b}_\tau(\mathbf{k}_\tau, \omega, z_d) = S_0 \left[\mathbf{Z}^+(\mathbf{k}_\tau, \omega, z_d) - \mathbf{Z}^-(\mathbf{k}_\tau, \omega, z_d)\right]^{-1} \mathbf{k}_\tau, \tag{8}$$

$$\mathbf{e}^\pm_\tau(\mathbf{k}_\tau, \omega, z_d) = \mathbf{Z}^\pm(\mathbf{k}_\tau, \omega, z_d)\mathbf{b}_\tau(\mathbf{k}_\tau, \omega, z_d). \tag{9}$$

Here $\mathbf{e}^\pm_\tau(\mathbf{k}_\tau, \omega, z_d) = \mathbf{e}_\tau(\mathbf{k}_\tau, \omega, z_d \pm 0)$, and the impedance matrices $\mathbf{Z}^+$ and $\mathbf{Z}^-$ at the level $z = z_d$ are found by the solution of Cauchy problem for matrix differential equation (A1) in Appendix A with boundary conditions, respectively, at infinity and at the ground.

Further, one can find the horizontal electromagnetic field components (spatial spectrum) $\mathbf{e}_\tau(\mathbf{k}_\tau, \omega, z)$ and $\mathbf{b}_\tau(\mathbf{k}_\tau, \omega, z)$ at any level z by solving the Cauchy problem for the system (4), (5) with boundary conditions (8) and (9) at the source level $z = z_d$. Herewith, quite naturally, for the solution at $z > (<) z_d$ the boundary value $\mathbf{e}^\pm_\tau(z_d)$ is to be used.

5. Spatial Distribution of ULF Electromagnetic Field Produced by a Dipole Source in the Atmosphere

To get the spatial distribution of magnetic horizontal components at any altitude z, we apply the inverse Fourier transform to the spatial spectrum $\mathbf{b}_\tau(\mathbf{k}_\tau, \omega, z)$, found in the previous section, namely,

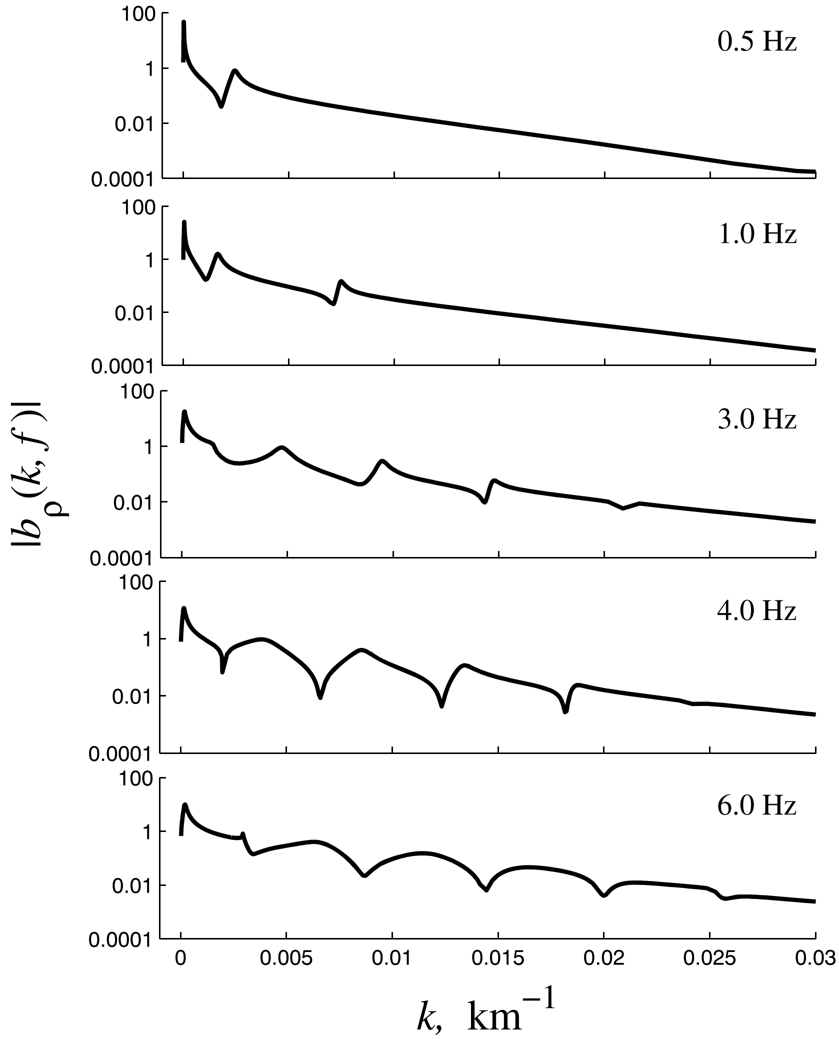

Figure 2. The dependence of radial magnetic harmonic $|b_\rho(k,f)|$ on wave vector $k \equiv k_\rho$ for several values of frequency f from 0.5 Hz to 6 Hz.

$\mathbf{b}_\tau(\rho,\omega,z) = (2\pi)^{-1}\int \mathbf{b}_\tau(\mathbf{k}_\tau,\omega,z)\exp(i\mathbf{k}_\tau\rho)\mathrm{d}\mathbf{k}_\tau$. We transfer to the polar coordinates in the horizontal plane at the altitude z, using the matrix of the rotation from a fixed basis to the local basis in a point (ρ,φ):

$$\mathbf{U}(\varphi) = \begin{pmatrix} \cos\varphi & \sin\varphi \\ -\sin\varphi & \cos\varphi \end{pmatrix}.$$

In a similar way the local polar coordinates in the plane of wave vectors $\mathbf{k}_\tau$ in a point (k,θ) can be used.

Now we find the components $b_\rho(\rho,\varphi,\omega,z)$ and $b_\varphi(\rho,\varphi,\omega,z)$ of the vector $\mathbf{b}_\tau(\rho,\omega,z)$ in a local basis via the components of the vector $\mathbf{b}_\tau(\mathbf{k}_\tau,\omega,z)$ in the same local basis, denoted as $b_k(k,\theta,\omega,z)$ and $b_\theta(k,\theta,\omega,z)$. Further on, we omit the parameters ω and z for brevity. The inverse Fourier transform in the polar coordinates explicitly looks like

$$\begin{pmatrix} b_\rho(\rho,\varphi) \\ b_\varphi(\rho,\varphi) \end{pmatrix} = (2\pi)^{-1}\mathbf{U}(\varphi)\int\limits_0^\infty k\,\mathrm{d}k\int\limits_0^{2\pi}\mathbf{U}(-\theta)\begin{pmatrix} b_k(k,\theta) \\ b_\theta(k,\theta) \end{pmatrix}\exp\left[ik\rho\cos(\theta-\varphi)\right]\mathrm{d}\theta.$$

Hence, introducing $\psi = \theta - \varphi$ and keeping in mind that $\mathbf{U}(\varphi)\mathbf{U}(-\theta) = \mathbf{U}(\varphi-\theta) = \mathbf{U}(-\psi)$, we find

$$b_\rho(\rho,\varphi) = (2\pi)^{-1}\int\limits_0^\infty k\mathrm{d}k\int\limits_0^{2\pi}\left[b_k(k,\theta)\cos\psi - b_\theta(k,\theta)\sin\psi\right]\exp\left(ik\rho\cos\psi\right)\mathrm{d}\psi,$$

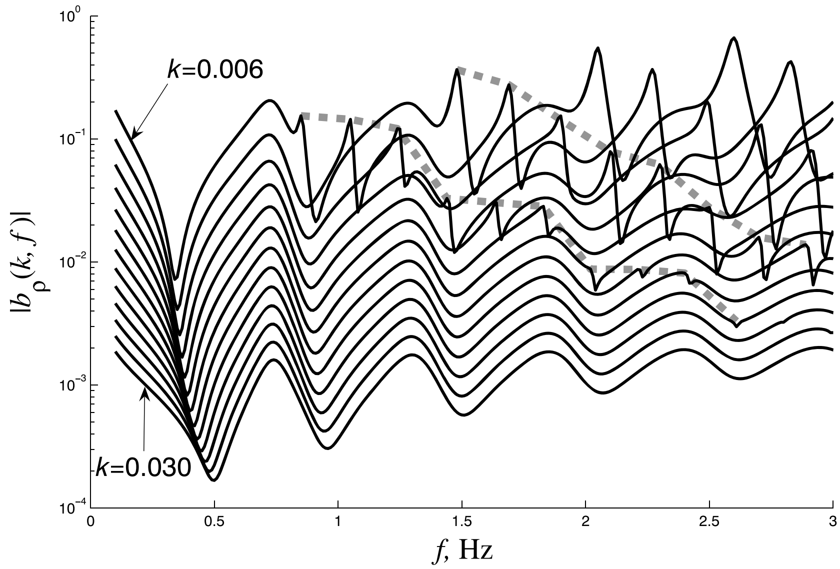

Figure 3. The frequency spectra $|b_\rho(f)|$ for various k from 0.006 km^{-1} to 0.030 km^{-1} with increment 0.002 km^{-1}. Maxima corresponding to the eigenfrequencies of FMS modes are marked by grey dashed lines.

$$b_\varphi(\rho,\varphi) = (2\pi)^{-1}\int_0^\infty k\mathrm{d}k\int_0^{2\pi}\left[b_k(k,\theta)\sin\psi + b_\theta(k,\theta)\cos\psi\right]\exp\left(ik\rho\cos\psi\right)\mathrm{d}\psi.$$

For high latitudes under consideration, the geomagnetic field inclination is $I = 90°$. Then, the components b_k and b_θ do not depend on angle θ; i.e., $b_k = b_k(k)$ and $b_\theta = b_\theta(k)$. Taking into account that an integral of antisymmetric function $\sin\psi\exp\left(ik\rho\cos\psi\right)$ vanishes, we obtain

$$\begin{pmatrix} b_\rho(\rho,\varphi) \\ b_\varphi(\rho,\varphi)\end{pmatrix} = \frac{1}{2\pi}\int_0^\infty \begin{pmatrix} b_k(k) \\ b_\theta(k)\end{pmatrix} k\mathrm{d}k\int_0^{2\pi}\cos\psi\exp\left(ik\rho\cos\psi\right)\mathrm{d}\psi = i\int_0^\infty k\begin{pmatrix} b_k(k) \\ b_\theta(k)\end{pmatrix} J_1(k\rho)\mathrm{d}k, \quad (10)$$

where $J_1(\dots)$ is the Bessel function of the first kind.

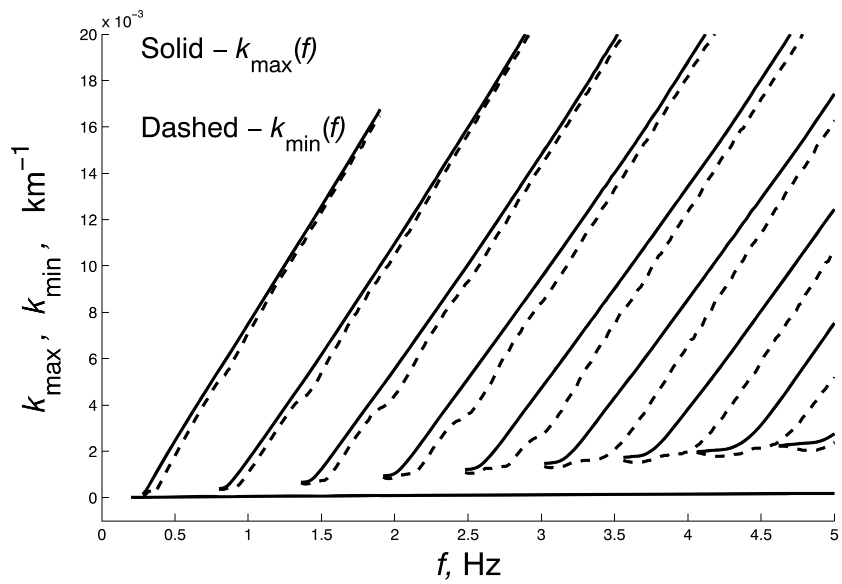

Figure 4. The dependence of maxima $k_{max}(f)$ (solid lines) and minima $k_{min}(f)$ (dashed lines) on frequency f of the $|b_\rho(k,f)|$ function.

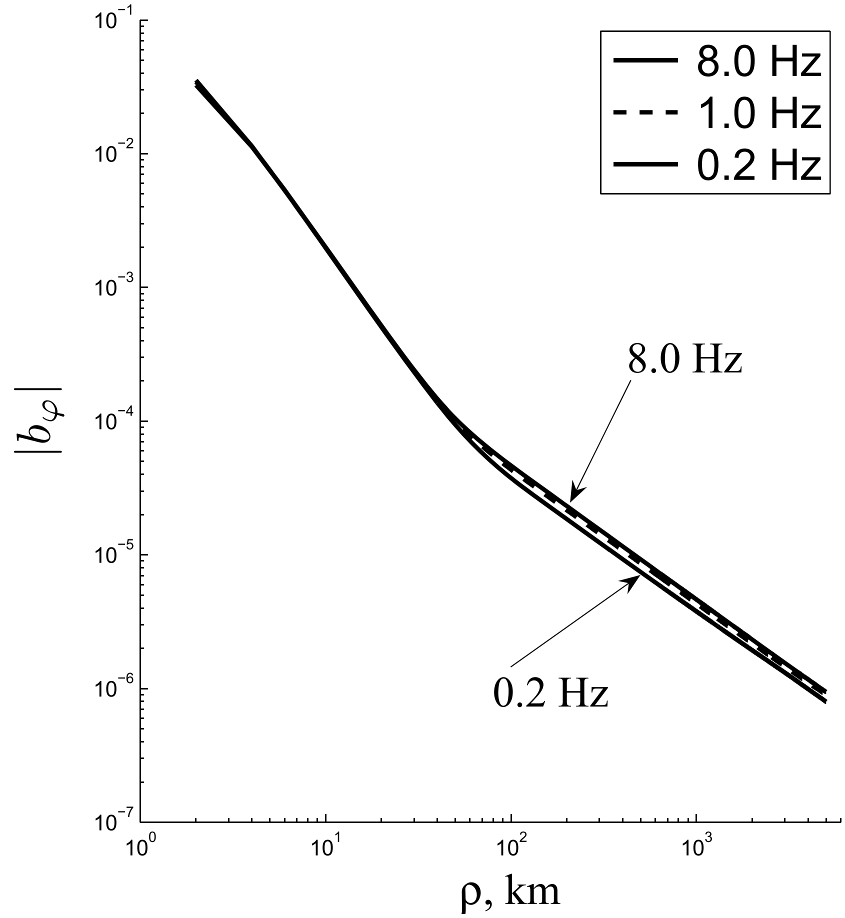

Figure 5. Variation of the b_φ magnetic component magnitude with distance ρ from an electric dipole at various frequencies.

From the relationship (10) a simple estimate can be obtained for the magnetic field. Let us consider a plane model of TM mode excitation in the Earth-ionosphere waveguide. The waveguide is limited by the ideally conductive Earth at $z = 0$ and the ionosphere's lower boundary at $z = h$. At short distances ρ from the source where $\rho \ll h$ the influence of the ionosphere is not significant. From (10) the well-known formula [*Wait*, 2013] for the magnetic field of a dipole above an infinitely conductive surface stems

$$b_\varphi(\rho, \omega) = \frac{\mu_0 M_C(\omega)}{2\pi\rho^2}. \tag{11}$$

If at altitude h there is an ideally conducting plane, then at $h \ll \rho \ll k_0^{-1}$ from (10) it follows that

$$b_\varphi(\rho, \omega) = \frac{\mu_0 M_C(\omega)}{2\pi\rho h}. \tag{12}$$

These simple relationships can be used for an easy evaluation of the expected ground magnetic response on lightning stroke.

6. Numerical Modeling

The results of numerical model are given below. The model provides spatial distributions on the ground ($z = 0$) of both azimuthal b_φ and radial b_ρ components of electromagnetic field produced by a vertical dipole in the atmosphere and spectra of magnetic disturbance at various distances ρ from a dipole. The altitude of the dipole source is assumed to be $z_d = 1$ km. The source magnitude is $M_Q = 10^6$ C m.

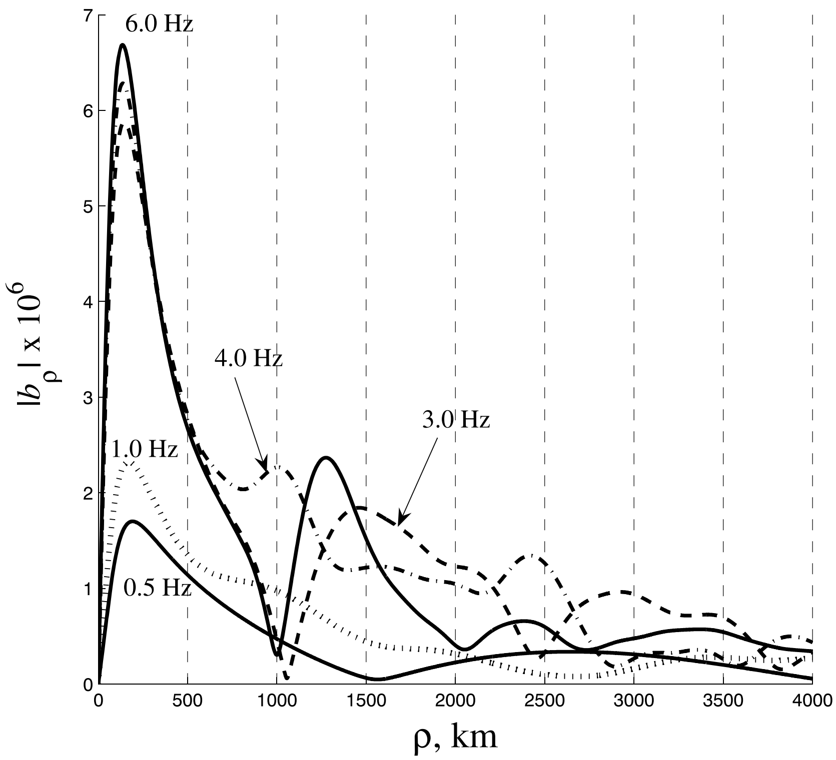

Figure 6. Variations of $b_\rho(\rho)$ with distance ρ for various f.

The IRI parameters correspond to the high-latitude station Barentsburg with coordinates: geographic latitude 78°, longitude 14.2°, MLT noon ~11 UT. As a typical example, we consider nighttime ionosphere (LT = 24) during 19 September 2010. The ground conductivity is assumed to be $\sigma_g = 0.001$ S/m. The atmospheric conductivity is $\sigma_a = 1.1 \cdot 10^{-14}$ S/m at the ground surface.

A numerical solution of Cauchy problem for the system (4), (5) as well as Cauchy problem for matrix Riccati equation (A1) was performed with the Runge-Kutta method of differential equation solution, implemented in the standard RKF45 code [*Forsythe et al.*, 1977].

6.1. Spatial Spectra $b_\rho(k)$ of Excited Electromagnetic Wave Structure on the Ground

The Fourier spatial harmonics of the horizontal electromagnetic field components at the ground level $z = 0$ have been calculated by solving Cauchy problem for the system (4), (5) with boundary conditions (8) and (9) at the source level $z_d = 1$ km, using the boundary value $\mathbf{e}_\tau^-(z_d)$ for the electric component. Figure 2 shows the dependence of radial magnetic harmonic amplitude $|b_\rho(k,f)|$ on wave vector $k \equiv k_\rho$ for several values of frequency from 0.5 Hz to 6 Hz. These plots demonstrate a narrow and high peak at $k \sim 10^{-4}$ km^{-1}, corresponding to the E mode of the Earth-ionosphere waveguide, which has a dispersion equation $\omega/k \sim c$, similar to the dispersion equation of free infinite space. The spectral maxima emerging upon the increase of frequency (from top to bottom panels) correspond to the waveguide FMS modes. Upon the frequency increase, these maxima shift to the right, decrease and disperse, and finally disappear. These Fourier–Bessel harmonics determine the scale of spatial variations of magnetic disturbance in radial direction.

The frequency spectra $|b_\rho(f)|$ for various k from 0.006 km^{-1} to 0.030 km^{-1} are shown in Figure 3. Maxima of dependence $|b_\rho(k,f)|$ for a fixed k are reached nearly at the eigenfrequencies of MHD modes in the ionosphere. Narrow spikes correspond to the waveguide FMS modes, and wide maxima correspond to the IAR modes. Maxima corresponding to the eigenfrequencies of FMS modes (marked by grey dashed lines) shift to the right upon an increase of k, whereas maxima corresponding to the IAR eigenfrequencies do not depend on k.

Figure 4 shows the mapping on k-f plane of points, corresponding to maxima $k_{\max}(f)$ (solid lines) and minima $k_{\min}(f)$ (dashed line) of the function $|b_\rho(k,f)|$. This figure can be interpreted as a series of dispersion curves. In the simple case of a plane-stratified IAR model these dispersion curves reduce to the solution of the

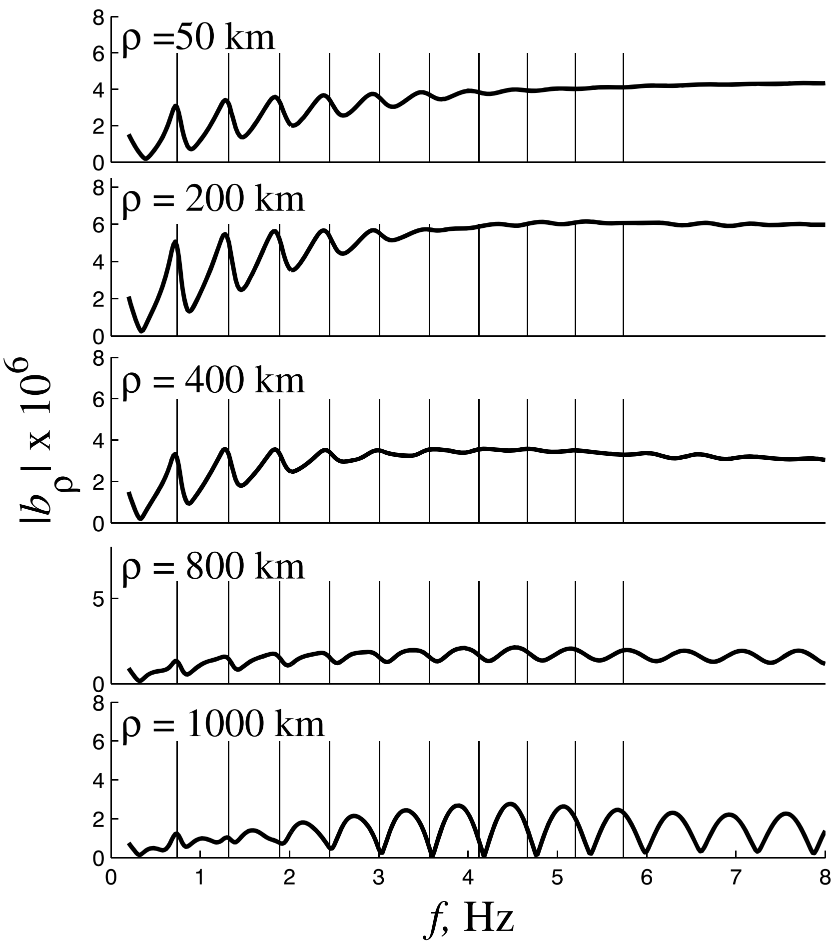

Figure 7. The spectra in the range 0.2–8.0 Hz at various distances from a source. Vertical dashed lines indicate IAR eigenfrequencies.

dispersion equation from *Surkov et al.* [2004]. The preliminary knowledge of $k_{max}(f)$ and $k_{min}(f)$ points facilitates greatly the numerical calculations and mode identification in a complicated spectral pattern. The $b_\rho(k)$ function rapidly varies in the vicinity of these points only, so inhomogeneous step along k is used: the program automatically decreases k net step only in the maxima and minima domains.

Nearly horizontal line in Figure 4 at $k \to 0$ corresponds to the atmospheric electric mode in the ionosphere-Earth waveguide. Inclined lines correspond to the k-f relationship for several harmonics of waveguide modes. These lines end in points where the difference between maximum and minimum vanishes. The same can be seen in Figure 3, where at the bottom curves corresponding to large k ($k > 0.024$ km^{-1}), narrow maxima associated with FMS modes vanish, so only smooth peaks associated to IAR modes remain.

6.2. Variation of the Magnetic Disturbance Magnitude With Distance

We present the magnitudes of magnetic disturbance for both azimuthal b_φ and radial b_ρ components for various frequencies in the range from 0.2 Hz to the Schumann resonance (8.0 Hz) at various distances from a vertical dipole, up to 4000 km.

Without the ionosphere, the magnetic ground response would be detected in the azimuthal b_φ component only. Variation of the $|b_\varphi(\rho)|$ magnetic component magnitude with distance ρ from an electric dipole at various frequencies is shown in Figure 5. The rate of the magnetic magnitude decay with distance is nearly the same for all frequencies in the band 0.2–8.0 Hz. The decay rate changes at $\rho \simeq 60$ km. This behavior is in good agreement with the predictions of simple relationships (11) and (12): the radial dependence changes from $\propto \rho^{-2}$ at small distances to $\propto \rho^{-1}$ at large distances. This change occurs at distances from a dipole about the height of the conductive layer of the atmosphere.

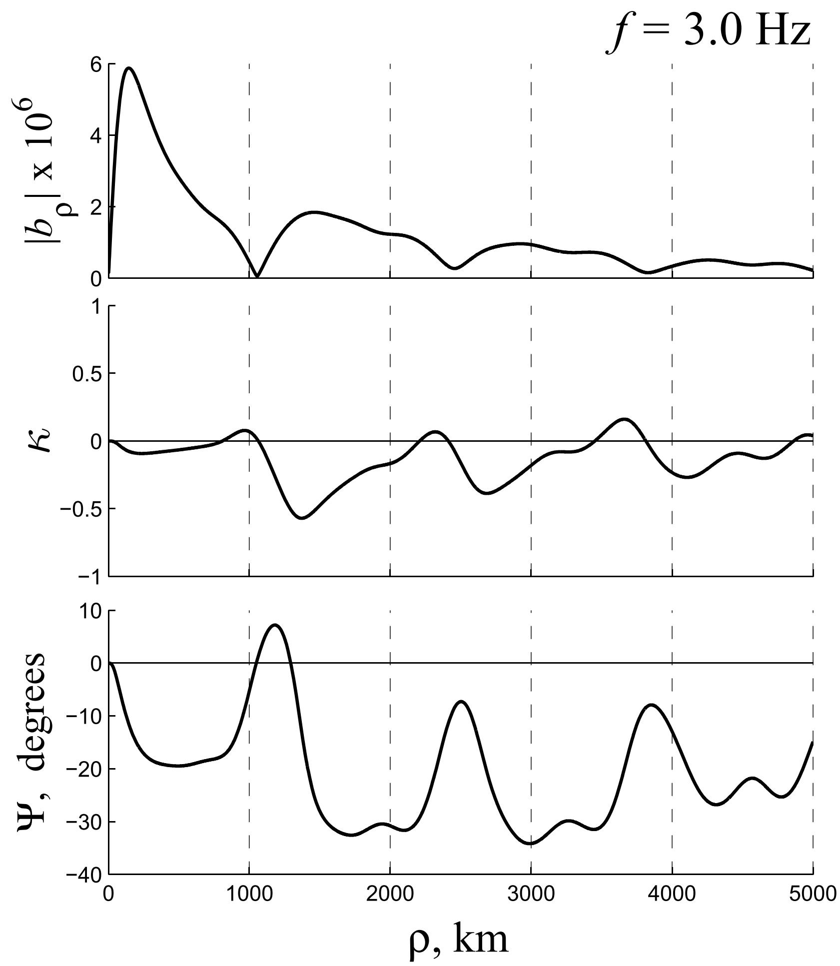

Figure 8. Variations with distance of polarization parameters $\kappa(\rho)$ and $\Psi(\rho)$ at frequency 3 Hz.

Though the radial b_ρ component is typically less than the azimuthal component b_φ, this component is more sensitive to the resonant properties of the ionosphere. Variations of $|b_\rho(\rho)|$ with distance for various f are shown in Figure 6. The spatial structure of b_ρ component demonstrates an interference pattern: the occurrence of periodic maxima and minima. The distance between subsequent minima/maxima corresponds to the wavelength of FMS mode, and it decreases with the increase of frequency. Though the field decay is non-monotonic, for some f it has no evident spatial periodicity. This complication arises owing to the interference pattern of several FMS waveguide modes.

6.3. Variation of Spectra With Distance

We present the spectra of horizontal magnetic components in the range 0.2–8.0 Hz at various distances from a source. The spectra of azimuthal $b_\varphi(f)$ component shows just a gradual increase of spectral power density with f in the band under consideration (not shown). The spectral resonant structure reveals itself in $b_\rho(f)$ component only (Figure 7). For a better physical insight we have indicated by vertical lines the IAR eigenfrequencies, preliminarily calculated for the chosen IRI parameters.

Nearby to the source ($\rho = 50$–400 km) only the lowest IAR harmonics are revealed: ~0.7, 1.3, 1.9, and 2.4 Hz. At higher frequencies, $f > 3$ Hz, a broadband enhancement occurs.

At distances $\rho > 400$ km the IAR spectral peaks are suppressed. Instead, spectral peaks at $f \geq 3.0$ Hz become more evident. Their frequencies do not match IAR eigenfrequencies, and they shift gradually to lower values upon the distance increase. These spectral peaks are associated with the FMS waveguide modes.

Finally, at $\rho = 1000$ km the spectral structure is dominated by peaks associated with the FMS waveguide modes: the spectral periodic peaks can be seen in the band $f > 2$ Hz.

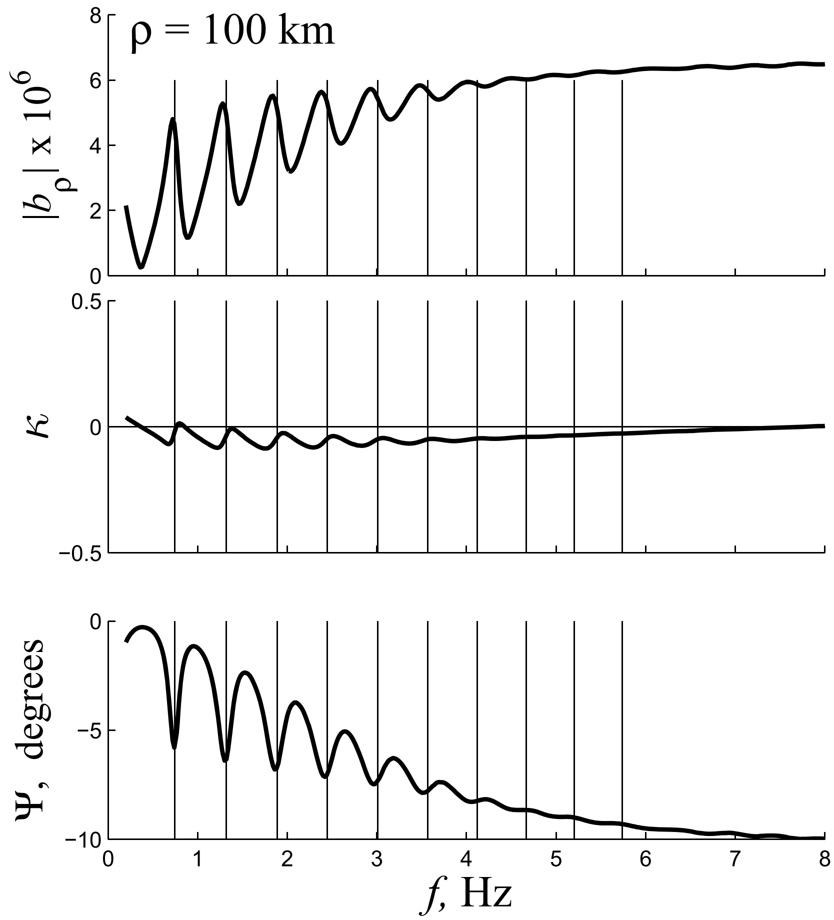

Figure 9. The polarization structure of the magnetic signal spectrum observed at small (100 km) distance from a source: (top) spectral amplitude $|b_\rho(f)|$, (middle) ellipticity $\kappa(f)$, and (bottom) orientation $\Psi(f)$. Vertical dashed lines indicate IAR eigenfrequencies.

Thus, multiple spectral peaks at $\rho \leq 400$ km are produced by the lowest 3–4 IAR harmonics, whereas at larger distances $\rho \geq 800$ km the multiple spectral peaks at $f > 2$ Hz are associated with waveguide modes. Here the numerical modeling results have been shown up to distances 10^3 km to demonstrate clearly the transition from the IAR-dominated spectral structure to the waveguide-dominated structure. At larger distances, $\sim(2-3) \cdot 10^3$ km, the spectral structure has a similar shape but with somewhat diminished amplitude.

6.4. Polarization Features

The resonant structure of b_ρ component is reflected in the behavior of polarization parameters: ellipticity κ, which is the signed ratio of minor polarization ellipse axis to its major axis, and ellipse orientation angle Ψ measured clockwise from x axis to the major ellipse axis. For the wavefield $b_{\rho,\varphi} \propto \exp(-i\omega t + \alpha_{\rho,\varphi})$ the ellipticity κ is determined by the formula $\kappa = s^{-1}\left(1 - \sqrt{1 - s^2}\right)$, where $s = 2|b_\rho b_\varphi|\left(|b_\rho|^2 + |b_\varphi|^2\right)^{-1} \sin\Phi$, and $\Phi = \alpha_\rho - \alpha_\varphi$ is the phase shift between the components. The sign $\kappa > 0/\kappa < 0$ corresponds to counterclockwise/clockwise rotation looking from above. The angle Ψ is found from the equation, $\tan(2\Psi) = 2|b_\rho b_\varphi|\left(|b_\rho|^2 - |b_\varphi|^2\right)^{-1} \cos\Phi$. The angle $\Psi = 0$ corresponds to the ellipse orientation perpendicular to the line source-observer, and $\Psi > 0/\Psi < 0$ corresponds to SE/SW quadrant.

The oscillatory decay of magnetic disturbance $|b_\rho(\rho)|$ is accompanied by oscillatory variations with distances of $\kappa(\rho)$ and $\Psi(\rho)$, shown in Figure 8 for $f = 3.0$ Hz. Extreme values of $\kappa(f)$ and $\Psi(f)$ are reached approximately at minima and maxima of amplitude spectrum $|b_\rho(\rho)|$. The polarization ellipse orientation is not directed strictly across the source-observation site line, but varies between −30° to 10°. Thus, the ellipse orientation in the ULF band cannot be used as a good indicator of the direction to a source.

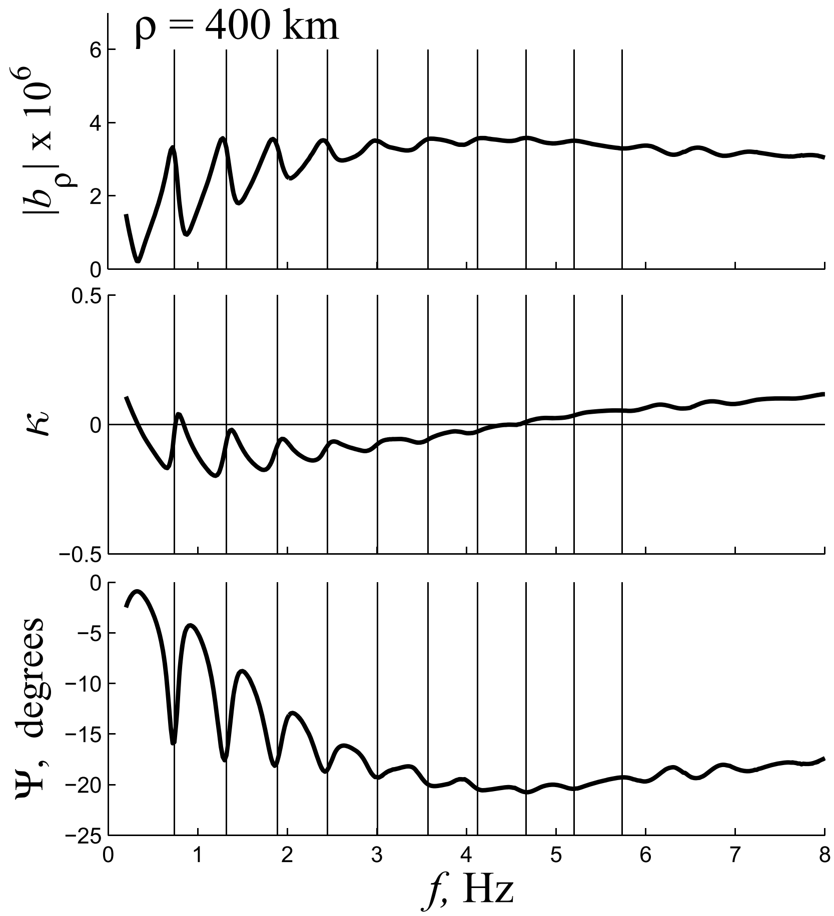

Figure 10. The polarization structure of the magnetic signal spectrum observed at medium (400 km) distances from a source: spectral amplitude $|b_\rho(f)|$, ellipticity $\kappa(f)$, and orientation $\Psi(f)$. Vertical dashed lines indicate IAR eigenfrequencies.

The polarization structure of the magnetic signal spectrum observed at various distances from a source is shown in Figures 9–11. In the vicinity of the source ($\rho = 100$ km, Figure 9) ellipticity $\kappa(f)$ is predominantly negative and weakly oscillates with frequency, though frequency modulation of amplitude spectrum $|b_\rho(f)|$ is clearly pronounced. The ellipticity tends to change sign at the frequency of a broad spectral maximum of $|b_\rho(f)|$. Upon increase of f, the ellipse orientation Ψ deviates from strictly azimuthal direction ($\Psi = 0$) but in an oscillatory way (Figure 9, bottom).

These oscillations become more evident at larger distances ($\rho = 400$ km, Figure 10). Ellipticity $\kappa(f)$ experiences change of sign, that is the change of the sense of rotation, at the frequency of a broad spectral maximum of $|b_\rho(f)|$. The ellipse orientation angle $\Psi(f)$ experiences strong deviations (up to ~20°) from strictly azimuthal orientation.

At distances $\rho \geq 800$ km (Figure 11), the periodic modulation of polarization parameters encompasses the frequency range from 1 Hz to 8 Hz, whereas small periodic oscillations of both $\kappa(f)$ and $\Psi(f)$ are due to FMS waveguide mode influence.

Thus, oscillatory resonant structure of magnetic spectra at fixed observational site is accompanied by oscillatory frequency dependence of the $\kappa(f)$ and $\Psi(f)$ parameters. So the oscillatory spectral structure can be seen not only in a power spectrum, but in polarization spectra as well. At small distances from a source, extreme values of $\kappa(\rho)$ and $\Psi(\rho)$ are observed at several first IAR eigenfrequencies. At larger distances, the IAR-associated spectral peaks become indiscernible, and periodic modulation of polarization spectra is caused by FMS waveguide frequencies. However, this modulation is not very deep. The polarization spectrum $\kappa(f)$

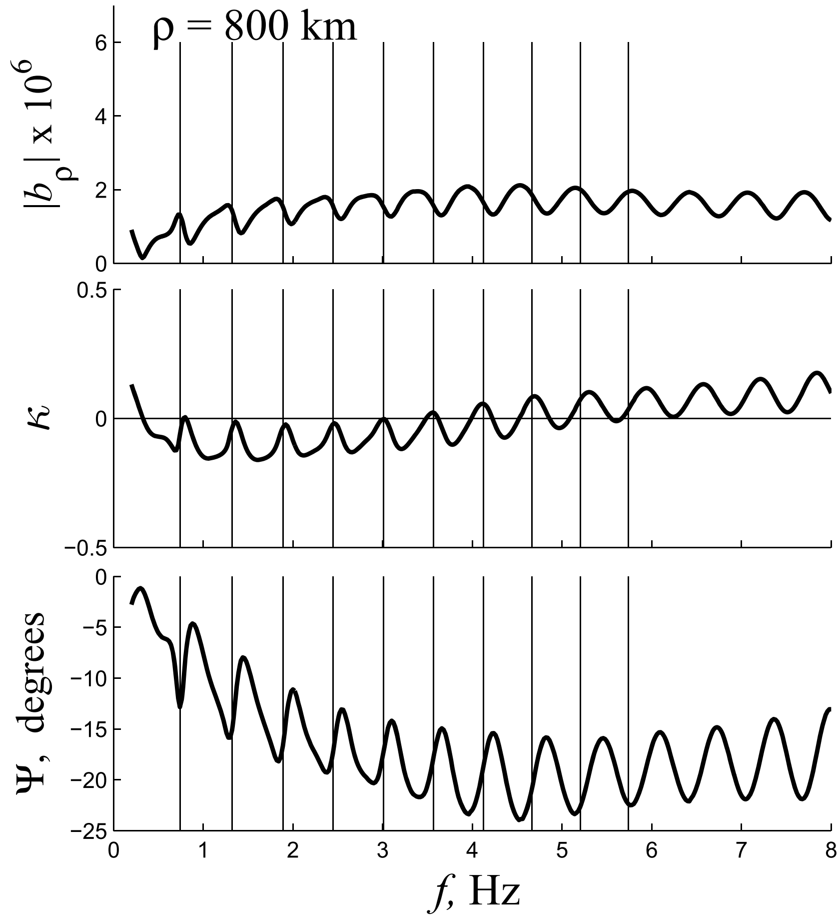

Figure 11. The polarization structure of the magnetic signal spectrum observed at large (800 km) distance from a source: spectral amplitude $|b_\rho(f)|$, ellipticity $\kappa(f)$, and orientation $\Psi(f)$. Vertical dashed lines indicate IAR eigenfrequencies.

should demonstrate a change of the ellipse rotation sense at some intermediate (dependent on a distance) frequency, corresponding to the broad maximum of spectral power.

6.5. Diurnal Variation for Two Seasons

Figure 12 shows overlapped spectra $|b_\rho(f)|$ for noon and midnight during winter (9 January 2010). Comparison of noon (dashed line) and midnight (solid line) responses shows that at $f \geq 4$ Hz nighttime response is larger than during daytime. Moreover, during the nominal nighttime (though the day under consideration corresponds to the polar night season) the periodic modulation of spectra is more evident.

The same comparison between noon and midnight on early autumn period (19 September 2010) shows even greater contrast (Figure 13). Comparison of spectra modulation at large distances (≥800 km) for winter (Figure 12) and autumn (Figure 13) periods shows the occurrence of seasonal effect: modulation depth during summer-autumn is more clearly pronounced than during winter.

7. Discussion

The theoretical modeling presented above has shown that atmospheric lightning discharges excite a complex system of coupled oscillations, consisting of the atmospheric E mode waveguide, ionospheric FMS waveguide, and IAR. In all earlier models of the IAR excitation by lightning flashes, the excitation of ionospheric FMS waveguide modes was not taken into account. Formally, in all calculations based on the *Sobchakov et al.* [2003] model the input impedance of the ionosphere was considered for modes with wave number $k = 0$ only, and its dependence on k was not taken into account.

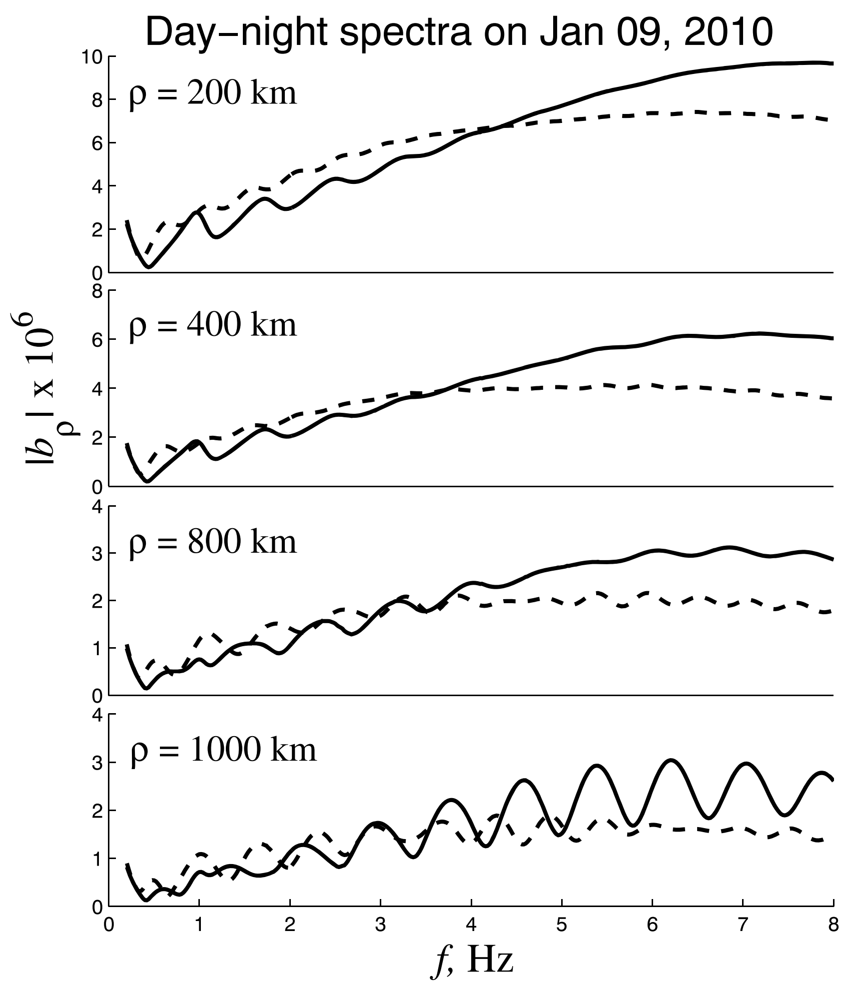

Figure 12. Comparison of spectra $b_\rho(f)$ between noon (dashed line) and midnight (solid line) during winter (9 January 2010) for various distances from a source.

High efficiency of FMS waveguide modes in the transfer of wave disturbances along the ionosphere to large distances is known from early studies. The numerical modeling with multilayered ionosphere in a vertical geomagnetic field of ionospheric waveguide excitation by incident magnetospheric Alfvén disturbances [*Greifinger and Greifinger*, 1968; *Fujita*, 1988] gave the following basic properties: the wave spatial attenuation was larger in the dayside ionosphere, and it was decreased at higher f; upon ducted wave propagation away from the geomagnetic plane the attenuation was larger as compared with the propagation in the meridional plane. These predictions were confirmed by multipoint observations and by more advanced numerical modeling [*Woodroffe and Lysak*, 2012].

Our modeling has shown that upon excitation of the ionosphere by an atmospheric source, at large distances from it (>400 km) the multiband spectral structure is formed owing to the waveguide modes, but not IAR. To validate this prediction, an examination of ULF response to lightning flashes at an array of high-sensitive search coil magnetometers would be necessary.

Some predictions of the IRI-based numerical model of the atmosphere-ionosphere excitation by lightning presented here match well-known facts. There is no thunderstorm activity on Svalbard, so all lightning sources must originate from Scandinavia and mainland Europe, or even from the African tropical center. However, a consideration in *Fedorov et al.* [2006] showed that thunderstorm centers in the tropics can hardly be a possible driver of ULF disturbance at high latitudes.

According to the modeling results, at distances ≥800 km from a stroke the genuine spectral peaks at IAR eigenfrequencies cannot be seen, and multiband spectral peaks can be associated only with waveguide FMS modes. The attenuation of these modes in the nightside ionosphere is to be much less than that in the daytime.

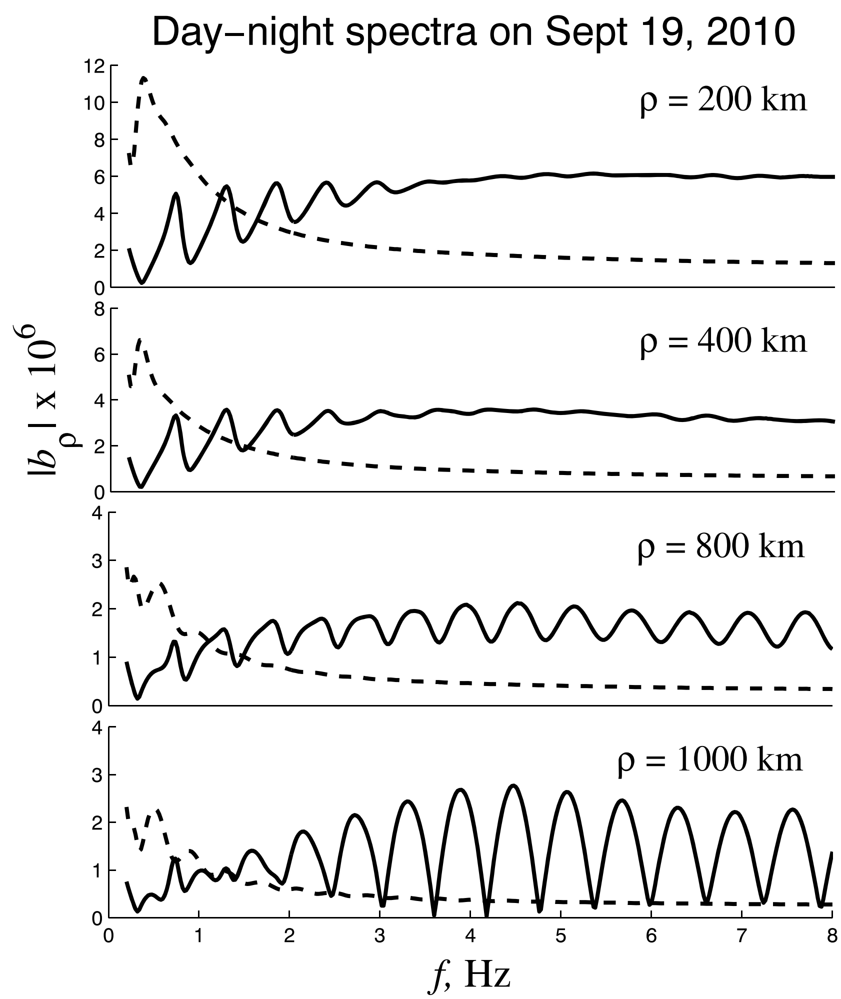

Figure 13. Comparison of spectra $b_\rho(f)$ between noon (dashed line) and midnight (solid line) on early autumn period (19 September 2010) for various distances from a source.

This theoretical prediction can explain the dominance of spectral structure occurrence on Svalbard during night hours, even during polar night periods. The numerical modeling based on the IRI model has also shown that during summer or early autumn, nighttime spectral features are more pronounced than during winter, in accord with observational facts.

The results of the numerical modeling have been presented for the case of the vertical geomagnetic field. In this case the mathematical apparatus and interpretation of numerical results are somewhat simplified. In particular, the ionospheric response does not depend on the angle between the geomagnetic meridian and direction to a source. However, the basic model conclusions, such as variations of the IAR and FMS waveguide contributions to the ground spectral structure with a distance from a source, can be qualitatively applied to middle latitudes as well. More detailed calculations for a specific midlatitude site will be provided elsewhere.

Though the model predictions do not contradict the results of IAR observations on Svalbard, a reliable model validation demands more dedicated experimental studies, using existing multiinstrument Svalbard facilities: the sensitive search coil magnetometer at Barentsburg (pgia.ru) and the EISCAT radar (www.eiscat.se).

8. Conclusion

The results of numerical modeling have shown that during the impact of the atmospheric electric discharge fields on the ionosphere, a combined system of local IAR and FMS waveguide modes is excited, which results in a complicated spectral structure of the response. For the frequency below the IAR range ($f < 1.0$ Hz) this radial magnetic component is weakly excited and decays nearly monotonically with distance ρ. At higher frequencies $f \geq 3$ Hz, the spatial structure of the radial $|b_\rho(\rho)|$ component demonstrates an interference pattern: the occurrence of periodic maxima and minima. The spectral peaks at $\rho \leq 400$ km are produced by lowest the 4–5 IAR harmonics, whereas at larger distances $\rho \geq$800 km the spectral peaks at $f > 2$ Hz are associated with FMS waveguide modes. The resonant structure of magnetic spectra at a fixed observational site is accompanied by an oscillatory frequency dependence of polarization parameters: ellipticity $\kappa(f)$ and ellipse orientation $\Psi(f)$. At small distances from a source, extreme values of $\kappa(\rho)$ and $\Psi(\rho)$ are observed at several first IAR eigenfrequencies. At larger distances the IAR-associated spectral peaks become indiscernible, and weak periodic modulation of polarization spectra is caused by FMS waveguide frequencies.

Appendix A: Electromagnetic Field at the Source Altitude via Impedance Matrix

Horizontal components of electric $\mathbf{e}_\tau$ and magnetic $\mathbf{b}_\tau$ fields are related by the impedance relationship (6). Substituting this relationship into the homogeneous system corresponding to the basic system (4), (5), we obtain

$$\partial_3 \mathbf{b}_\tau = \mathbf{T}_{\mathrm{bb}} \mathbf{b}_\tau + \mathbf{T}_{\mathrm{be}} \mathbf{Z} \mathbf{b}_\tau, \qquad (\partial_3 \mathbf{Z}) \mathbf{b}_\tau + \mathbf{Z} \partial_3 \mathbf{b}_\tau = \mathbf{T}_{\mathrm{eb}} \mathbf{b}_\tau + \mathbf{T}_{\mathrm{ee}} \mathbf{Z} \mathbf{b}_\tau.$$

Substituting $\partial_3 \mathbf{b}_\tau$ from the first equation of the latter system into the second equation, we get

$$\left(\partial_3 \mathbf{Z} + \mathbf{Z} \mathbf{T}_{\mathrm{be}} \mathbf{Z} + \mathbf{Z} \mathbf{T}_{\mathrm{bb}} - \mathbf{T}_{\mathrm{ee}} \mathbf{Z} - \mathbf{T}_{\mathrm{eb}} \right) \mathbf{b}_\tau = 0.$$

The latter equation is valid for any solution of the system (4), (5) under the condition

$$\partial_3 \mathbf{Z} = -\mathbf{Z} \mathbf{T}_{\mathrm{be}} \mathbf{Z} - \mathbf{Z} \mathbf{T}_{\mathrm{bb}} + \mathbf{T}_{\mathrm{ee}} \mathbf{Z} + \mathbf{T}_{\mathrm{eb}}. \tag{A1}$$

This generalized matrix Riccati equation is used to find the impedance matrices $\mathbf{Z}^+$ and $\mathbf{Z}^-$ in (8) and (9).

Now we obtain the relationships describing the electric and magnetic field of a dipole at the altitude of a source $z = z_d$ via the impedance matrices. The matrix $\mathbf{Z}^-$ is derived from the transfer of the boundary condition (6) from the ground $z = 0$ to the source $z = z_d$, whereas the matrix $\mathbf{Z}^+$ stems from the transfer of the emission condition downward to the source level $z = z_d$. Functions with plus sign correspond to two linearly independent solutions of (4) and (5), satisfying the emission condition at $z \to \infty$, and those with minus sign correspond to solutions of (4) and (5), satisfying the boundary condition on the ground:

$$\mathbf{f}_1^\pm = \begin{pmatrix} \mathbf{b}_1^\pm \\ \mathbf{e}_1^\pm \end{pmatrix}, \qquad \mathbf{f}_2^\pm = \begin{pmatrix} \mathbf{b}_2^\pm \\ \mathbf{e}_2^\pm \end{pmatrix}.$$

Solutions above and beneath the source can be presented, respectfully, as $\mathbf{b}_\tau^\pm = \mathbf{B}^\pm \mathbf{C}^\pm$ and $\mathbf{e}_\tau^\pm = \mathbf{E}^\pm \mathbf{C}^\pm$, where the matrices $\mathbf{B}^\pm = \left(\mathbf{b}_1^\pm, \mathbf{b}_2^\pm \right)$ and $\mathbf{E}^\pm = \left(\mathbf{e}_1^\pm, \mathbf{e}_2^\pm \right)$ act on 2-D vector columns $\mathbf{C}^\pm$ of arbitrary constants. From boundary condition (7) it follows that

$$\mathbf{B}_d^+ \mathbf{C}^+ - \mathbf{B}_d^- \mathbf{C}^- = 0, \qquad \mathbf{E}_d^+ \mathbf{C}^+ - \mathbf{E}_d^- \mathbf{C}^- = S_0 \mathbf{k}_\tau,$$

where $\mathbf{B}_d^\pm = \mathbf{B}^\pm(z_d)$, and $\mathbf{E}_d^\pm = \mathbf{E}^\pm(z_d)$. From above the following relationship stems

$$(\mathbf{Z}^+ - \mathbf{Z}^-) \mathbf{B}_d^+ \mathbf{C}^+ = S_0 \mathbf{k}_\tau, \tag{A2}$$

where $\mathbf{Z}^\pm = \mathbf{E}_d^\pm \left(\mathbf{B}_d^\pm \right)^{-1}$ are impedance matrices above (+) and beneath (−) a dipole. The harmonic of horizontal magnetic field is continuous at $x^3 = z_d$; therefore, at the source level $\mathbf{b}_\tau(z_d) = \mathbf{B}_d^+ \mathbf{C}^+ = \mathbf{B}_d^- \mathbf{C}^-$. From (A2), calculating preliminarily the inverse matrix $(\mathbf{Z}^+ - \mathbf{Z}^-)^{-1}$, one can find the desired $\mathbf{b}_\tau(z_d)$ in the form of the relationship (8).

Appendix B: Coefficients of the System (4), (5)

The elements of the matrices $\mathbf{T}^{\mathrm{bb}}$, $\mathbf{T}^{\mathrm{be}}$, $\mathbf{T}^{\mathrm{eb}}$ and $\mathbf{T}^{\mathrm{ee}}$ are as follows:

$$T_{11}^{\mathrm{bb}} = ik_1 \cot I - \overline{g} k_2 \cos I, \qquad T_{12}^{\mathrm{bb}} = \overline{g} k_1 \cos I,$$

$$T_{21}^{\mathrm{bb}} = \left(1 - \overline{\varepsilon}_\perp \right) ik_2 \cot I, \qquad T_{22}^{\mathrm{bb}} = \overline{\varepsilon}_\perp ik_1 \cot I,$$

$$T_{11}^{\mathrm{be}} = -\frac{i}{k_0}\left[k_1k_2 + i\frac{k_0^2 g}{\sin I}\left(1-\bar{\varepsilon}_\perp\cos^2 I\right)\right],$$

$$T_{12}^{\mathrm{be}} = \frac{i}{k_0}\left[k_1^2 - k_0^2\left(\varepsilon_\perp - g\bar{g}\cos^2 I\right)\right],$$

$$T_{21}^{\mathrm{be}} = -\frac{i}{k_0}\left[k_2^2 - k_0^2\frac{\varepsilon_\perp}{\sin^2 I}\left(1-\bar{\varepsilon}_\perp\cos^2 I\right)\right],$$

$$T_{22}^{\mathrm{be}} = \frac{i}{k_0}\left[k_1k_2 - i\frac{k_0^2 g}{\sin I}\left(1-\bar{\varepsilon}_\perp\cos^2 I\right)\right],$$

$$T_{11}^{\mathrm{eb}} = \frac{ik_1k_2}{k_0\varepsilon_{zz}}, \qquad T_{12}^{\mathrm{eb}} = ik_0\left(1-\frac{k_1^2}{k_0^2\varepsilon_{zz}}\right),$$

$$T_{21}^{\mathrm{eb}} = -ik_0\left(1-\frac{k_2^2}{k_0^2\varepsilon_{zz}}\right), \qquad T_{22}^{\mathrm{eb}} = -i\frac{k_1k_2}{k_0\varepsilon_{zz}},$$

$$T_{11}^{\mathrm{ee}} = ik_1\bar{\varepsilon}_\perp\cot I, \qquad T_{12}^{\mathrm{ee}} = k_1\bar{g}\cos I,$$

$$T_{21}^{\mathrm{ee}} = -ik_2\cot I\left(1-\bar{\varepsilon}_\perp\right), \qquad T_{22}^{\mathrm{ee}} = ik_1\cot I + k_2\bar{g}\cos I.$$

Here we use the notations $\bar{\varepsilon}_\perp = \varepsilon_\perp/\varepsilon_{zz}$, $\bar{g} = g/\varepsilon_{zz}$, and $\varepsilon_{zz} = \varepsilon_\perp\cos^2 I + \varepsilon_\parallel\sin^2 I$. Source vectors in (4), (5) are as follows:

$$\mathbf{s}_b = \frac{\mu_0 M_C(\omega)}{2\pi\varepsilon_{zz}}\begin{pmatrix} ig\cos I \\ \left(\varepsilon_\parallel - \varepsilon_\perp\right)\sin I\cos I\end{pmatrix}, \qquad \mathbf{s}_e = \frac{\mu_0 M_C(\omega)}{2\pi k_0\varepsilon_{zz}}\mathbf{k}_\tau .$$

Acknowledgments
This work was supported by the grant 246725 "Multi-Instrument Studies of High Latitude Atmospheric Turbulence and Wave Processes" from the POLARPROG program of the Norwegian Research Council (V.P., N.M., and L.B.) and RFBR grant 15-55-45064 (E.F.). Useful discussions with E. Ermakova and A. Sinha, as well as helpful comments from both reviewers, are appreciated. The IRI model code providing the ionospheric electron density, electron and ion temperatures, and ion composition is distributed by the NASA's Space Physics Data Facility (http://iri.gsfc.nasa.gov).

References

Baru, N. A., A. V. Koloskov, Y. M. Yampolski, and A. Y. Pashinin (2014), Evaluation technique for the $F2$ layer critical frequency by the difference of ionosphere Alfvén resonance eigenfrequencies, *Radiophys. Radioastron.*, *19*, 151–159.

Belyaev, P. P., S. V. Polyakov, V. O. Rapoport, and V. Y. Trakhtengerts (1989), Theory for the formation of resonance structure in the spectrum of atmospheric electromagnetic background noise in the range of short-period geomagnetic pulsations, *Radiophys. Quantum Electron.*, *32*, 802–810.

Bilitza, D., and B. Reinisch (2008), International reference ionosphere 2007: Improvements and new parameters, *Adv. Space Res.*, *42*, 599–609.

Bösinger, T., C. Haldoupis, P. P. Belyaev, M. N. Yakunin, N. V. Semenova, A. G. Demekhov, and V. Angelopoulos (2002), Spectral properties of the ionospheric Alfvén resonator observed at a low-latitude station (L = 1.3), *J. Geophys. Res.*, *107*(A10), 1281, doi:10.1029/2001JA005076.

Bösinger, T., A. Mika, S. L. Shalimov, C. Haldoupis, and T. Neubert (2006), Is there a unique signature in the ULF response to sprite-associated lightning flashes?, *J. Geophys. Res.*, *111*, A10310, doi:10.1029/2006JA011887.

Bösinger, T., E. N. Ermakova, C. Haldoupis, and D. Kotik (2009), Inclination effects in the spectral resonance structure of the ionospheric Alfvén resonator, *Ann. Geophys.*, *27*, 1313–1320.

Budden, K. G. (1966), *Radio Wave in the Ionosphere*, 542 p., Cambridge Univ. Press, Cambridge, U. K.

Demekhov, A. G. (2012), Coupling at the atmosphere-ionosphere-magnetosphere interface and resonant phenomena in the ULF range, *Space Sci. Rev.*, *168*, 595–609.

Ermakova, E. N., D. S. Kotik, S. V. Polyakov, and A. V. Shchennikov (2007), On a mechanism forming a broadband maximum in the spectrum of background noise at frequencies 2–6 Hz, *Radiophys. Quantum Electron.*, *50*, 555–569.

Ermakova, E. N., D. S. Kotik, and S. V. Polyakov (2008), Studying specific features of the resonance structure of the background noise spectrum in the frequency range 1–10 Hz with allowance for the slope of the Earth's magnetic field, *Radiophys. Quantum Electron.*, *51*, 519–527.

Ermakova, E. N., S. V. Polyakov, and D. S. Kotik (2010), Studying spectral structures in the background ultra-low-frequency noise at different latitudes, *Radiophys. Quantum Electron.*, *53*, 557–568.

Fedorov, E. N., A. J. Schekotov, O. A. Molchanov, M. Hayakawa, V. V. Surkov, and V. A. Gladyshev (2006), An energy source for the mid-middle latitudes IAR: World thunderstorm centers, nearby discharges or neutral wind fluctuations?, *Phys. Chem. Earth*, *31*, 462–468.

Fedorov, E., A. Schekotov, Y. Hobara, R. Nakamura, N. Yagova, and M. Hayakawa (2014), The origin of spectral resonance structures of the ionospheric Alfvén resonator: Single high-altitude reflection or resonant cavity excitation?, *J. Geophys. Res. Space Physics*, *119*, 3117–3129, doi:10.1002/2013JA019428.

Fedorov, E., N. Mazur, V. Pilipenko, and E. Ermakova (2016), Modeling diurnal variations of the IAR parameters, *Acta Geoda. Geophys.*, 1–21, doi:10.1007/s40328-015-0158-9.

Forsythe, G. E., M. A. Malcolm, and C. B. Moler (1977), *Computer Methods for Mathematical Computation*, Prentice-Hall, Englewood Cliffs, N. J.

Fujita, S. (1988), Duct propagation of hydromagnetic waves in the upper ionosphere. 2. Dispersion characteristics and loss mechanism, *J. Geophys. Res.*, *93*, 14,674–14,682.

Ginzburg, V. L. (1970), *The Propagation of Electromagnetic Waves in Plasmas*, Pergamon Press, Oxford, U. K.

Greifinger, C., and S. Greifinger (1968), Theory of hydromagnetic propagation in the ionospheric waveguide, *J. Geophys. Res.*, *76*, 7473–7490.

Lysak, R. L., C. L. Waters, and M. D. Sciffer (2013), Modeling of the ionospheric Alfvén resonator in dipolar geometry, *J. Geophys. Res. Space Physics*, *118*, 1514–1528, doi:10.1002/jgra.50090.

Mursula, K., K. Prikner, F. Z. Feygin, T. Braysy, J. Kangas, R. Kertulla, P. Pollari, T. Pikkarainen, and O. A. Pokhotelov (2000), Nonstationary Alfvén resonator: New results on Pc1 pearls and IPDP events, *J. Atmos. Sol. Terr. Phys.*, *62*, 299–309.

Nickolaenko, A. P., and M. Hayakawa (2002), *Resonances in the Earth-Ionosphere Cavity*, Klumer Acad., Dordrecht, Boston and London.

Nickolaenko, A. P., Y. P. Galuk, and M. Hayakawa (2015), Vertical profile of atmospheric conductivity corresponding to Schumann resonance parameters, *Telecomm. Radio Eng.*, *74*, 1483–1495.

Polyakov, S. V., and V. O. Rapoport (1981), The ionospheric Alfvén resonator, *Geomagn. Aeron.*, *21*, 610–614.

Polyakov, S. V., E. N. Ermakova, A. S. Polyakov, and M. N. Yakunin (2003), Formation of the spectra and polarization of background ULF electromagnetic noise at the Earth's surface, *Geomagn. Aeron.*, *42*, 240–248.

Pilipenko, V. A., O. M. Chugunova, M. J. Engebretson, and M. Lessard (2011), Trans-polar propagation of Pi1 wave burst as observed by an Antarctic array during the Themis 2007/03/23 substorm, paper presented at 34th Annual Seminar "Physics of Auroral Phenomena", pp. 86–89, Apatity, Russia.

Pilipenko, V. A. (2012), Impulsive coupling between the atmosphere and ionosphere/magnetosphere, *Space Sci. Rev.*, *168*, 533–550.

Potapov, A. S., T. N. Polyushkina, B. V. Dovbnya, B. Tsegmed, and R. A. Rakhmatulin (2014), Emissions of ionospheric Alfvén resonator and ionospheric conditions, *J. Atmos. Sol. Terr. Phys.*, *119*, 91–101.

Semenova, N. V., and A. G. Yahnin (2008), Diurnal behavior of the ionospheric Alfvén resonator signatures as observed at high latitude observatory Barentsburg ($L = 15$), *Ann. Geophys.*, *26*, 2245–2251.

Semenova, N. V., A. G. Yahnin, A. N. Vasilev, and O. Amm (2008), Specific features of resonance structures in spectra of ULF electromagnetic noise at high latitudes (Barentsburg Observatory), *Geomagn. Aeron.*, *48*, 36–44.

Shalimov, S., and T. Bösinger (2008), On distant excitation of the ionospheric Alfvén resonator by positive cloud-to-ground lightning discharges, *J. Geophys. Res.*, *113*, A02303, doi:10.1029/2007JA012614.

Shindo, T., and M. A. Uman (1989), Continuing current in negative cloud-to-ground lightning, *J. Geophys. Res.*, *94*(D4), 5189–5198.

Sobchakov, L. A., S. V. Polyakov, and N. L. Astakhova (2003), Excitation of electromagnetic waves in a plane waveguide with anisotropic upper wall, *Radiophys. Quantum Electron.*, *46*, 1503–1510.

Sukhorukov, A. I., and P. Stubbe (1997), Excitation of the ionospheric Alfvén resonator by strong lightning discharges, *Geophys. Res. Lett.*, *24*, 829–832.

Surkov, V., and M. Hayakawa (2014), *Ultra and Extremely Low Frequency Electromagnetic Fields, Springer Geophys. Ser.*, vol. 16, 486 pp., Springer, Japan.

Surkov, V. V., O. A. Pokhotelov, M. Parrot, E. N. Fedorov, and M. Hayakawa (2004), Excitation of the ionospheric resonance cavity by neutral winds at middle latitudes, *Ann. Geophys.*, *22*, 2877–2889.

Surkov, V. V., O. A. Molchanov, M. Hayakawa, and E. N. Fedorov (2005), Excitation of the ionospheric resonance cavity by thunderstorms, *J. Geophys. Res.*, *110*, A04308, doi:10.1029/2004JA010850.

Surkov, V. V., M. Hayakawa, A. Y. Schekotov, E. N. Fedorov, and O. A. Molchanov (2006), Ionospheric Alfvén resonator excitation due to nearby thunderstorms, *J. Geophys. Res.*, *111*, A01303, doi:10.1029/2005JA011320.

Trakhtengertz, V. Y., A. C. Demekhov, P. P. Belyaev, S. V. Polyakov, E. N. Ermakova, and S. V. Isaev (2000), A mechanism of anticorrelation in the occurrence of ULF electromagnetic noise resonance structure and Pc1 magnetic pulsations through the solar activity cycle, *J. Atmos. Sol. Terr. Phys.*, *62*, 253–256.

Wait, J. R. (2013), *Electromagnetic Waves in Stratified Media*, 620 pp., Elsevier, New York.

Woodroffe, J. R., and R. L. Lysak (2012), Ultra-low frequency wave coupling in the ionospheric Alfvén resonator: Characteristics and implications for the interpretation of ground magnetic fields, *J. Geophys. Res.*, *117*, A03223, doi:10.1029/2011JA017057.